International Journal of GEOMATE, Jan., 2024 Vol.26, Issue 113, pp.50-57
ISSN: 2186-2982 (P), 2186-2990 (O), Japan, DOI: https://doi.org/10.21660/2024.113.g13179
Geotechnique, Construction Materials and Environment

PAVEMENT-TIRE CONTACT PATCH EFFECTS ON AIR VOLUME USING FINITE ELEMENT METHOD

Thanat Saisaengtham[1,3], Juthanee Phromjan[1,3], Ravivat Rugsaj[2], Siwakorn Phakdee[1,3] and Chakrit Suvanjumrat[1,3]*

[1]Department of Mechanical Engineering, Faculty of Engineering, Mahidol University, Salaya, Nakhon Pathom 73170, Thailand;
[2]Department of Mechatronics Engineering and Artificial Intelligence, Vincent Mary School of Engineering, Assumption University, Samut Prakan 10570, Thailand;
[3]Laboratory of Computer Mechanics for Design (LCMD), Department of Mechanical Engineering, Faculty of Engineering, Mahidol University, Salaya, Nakhon Pathom 73170, Thailand;

*Corresponding Author, Received: 13 June 2023, Revised: 12 Nov. 2023, Accepted: 15 Dec. 2023

ABSTRACT: The investigation into the noise generated by automotive tires delves into various mechanisms, such as tire vibration, adhesion, and the notably significant air-pumping mechanism. This particular mechanism stems from the rapid compression and expulsion of air within the tire-pavement contact patch, a result of the deformation of the tire tread. The study employs the finite element method to scrutinize tire deformation and quantify the air volume at the contact patch, forming the primary objective of the research. To benchmark the composite pneumatic tire model, vertical stiffness and footprint tests are conducted on the pneumatic tire. The validation of the automotive tire model reveals an average error of 6.47% for vertical displacement and 15.89% for footprint area. Additionally, variations in vertical load and inflation pressure are examined to observe their impact on air volume. The study proposes a mathematical model illustrating the relationship between air volume, vertical load, and inflation pressure. This mathematical model is deemed valuable and holds potential applications for reducing air-pumping noise in future endeavors.

Keywords: Tire, Tire tread, Air volume, Contact patch, Finite element method

1. INTRODUCTION

The noise levels in the Bangkok metropolitan region of Thailand have experienced an increase, with a significant contribution from noise pollution generated by vehicle tires. According to Nillson et al. [1], tire-generated noise can be classified into two mechanisms—structure and airborne—linked to tire structure and the movement of air during travel, involving aspects like vibration and air-pumping. These mechanisms are particularly relevant to the tire-pavement interaction area, known as the contact patch.

Researchers have explored various methodologies, including experiments, computer-aided design (CAD), and computer-aided engineering (CAE), to investigate and enhance tire noise reduction. Li et al. [2] classified models for tire-pavement interaction noise into deterministic, statistical, and hybrid models. Several experimental approaches have been used to study tire noise mechanisms. For example, Keijiro et al. [3] used a chassis dynamometer to simulate tire movement on the road and analyze tire noise generation. Okan Sirin et al. [4] conducted on-road vehicle tests, collecting noise data at the tire-pavement interface to examine factors influencing tire noise. Gautam et al. [5] employed drum testing with microphones in an anechoic chamber to delve into tire noise. However, studying the air-related mechanism proves challenging in experiments as they encompass both structure and airborne mechanisms simultaneously. Spies et al. [6] developed two artificial neural networks (ANNs) to predict the tread pattern and the non-tread pattern related noise components of tire noise, separately. The major inputs of the tread pattern were the coherent tread profile spectrum and the air volume velocity spectrum calculated from the digitized 3D tread pattern. The major input of the non-tread pattern was the tread rubber hardness. The vehicle speed is also included as input for the two ANNs.

In the contemporary era, the considerable computational power offered by computer resources has significantly enhanced calculation performance. CAE plays a pivotal role in tire noise research, capitalizing on these capabilities. Bassill et al. [7] utilized a numerical model based on the finite volume method (FVM) to explore the impact of speed on tire noise. Zhou et al. [8] adopted a numerical model combining FVM with the FEM to investigate how tire load, inflation pressure, and rolling speed affect the air-pumping noise mechanism, specifically associated with the volume of airflow within deformed tire grooves. The FEM proves instrumental in understanding the characteristics of pneumatic tires' contact patches and tire deformations under varying load and inflation pressure conditions. Consequently, there is a keen interest in utilizing a comprehensive FEM approach to examine parameters influencing the air-pumping mechanism. For instance, Liang Chen et al. [9], much like Shuiting Zhou et al. [10], employed FEM simulations to scrutinize the behavior of the tire's contact patch under different parameters. Similarly, Phromjan and Suvanjumrat [11, 12] delved into the contact patch characteristics of solid tires using FEM, developing a 3D finite element (FE) model to simulate the footprint area, revealing the shape and distribution of the contact area for solid tires. Consequently, the pavement-tire contact patch is significant in generating tire noise.

2. RESEARCH SIGNIFICANCE

This study investigates the impact of tire-pavement interaction on air volume in the contact patch area under varying vertical loads and inflation pressures. Using a FE model, it simulates composite pneumatic tire deformation, extracting air volume in the groove. Acting as a preliminary criterion, the model offers foundational insights into the air-pumping noise generation mechanism. It sets the stage for future studies exploring intricate details and advanced numerical models to comprehensively understand air-pumping noise.

3. MATERIAL TESTING

The tensile and compression tests were conducted to assign element properties for the sidewall and tread models, respectively. For the sidewall testing, dumbbell-shaped specimens in accordance with ASTM D412 Test (Die C) were prepared, featuring a gauge length of 25 mm. On the other hand, circular cylinder specimens with a diameter of 28.6 mm and a thickness of 12.5 mm were prepared for tread testing following ASTM D575 standards. Figure 1 illustrates these specimens as samples. The material properties testing was carried out using a universal testing machine (Model 5556, INSTRON), as depicted in Figure 2.

4. TIRE TESTING

In this study, a 205/65 R15 pneumatic tire was utilized and subjected to a vertical stiffness tester to validate the finite element model of tire deformation. The tests were specifically designed to analyze the tire's vertical displacements and observe the behavior of the contact patch under different vertical loads while adhering to the recommended inflation pressure of 220 kPa. The vertical stiffness tests were conducted using the EKTRON TEK model PL-2003 vertical stiffness tester at the Research and Development Center for Thai Rubber Industry (RDCTRI), providing a controlled environment for accurate and systematic examination.

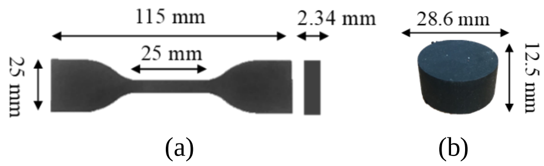

Fig. 1 Material specimens of (a) sidewall and (b) tread

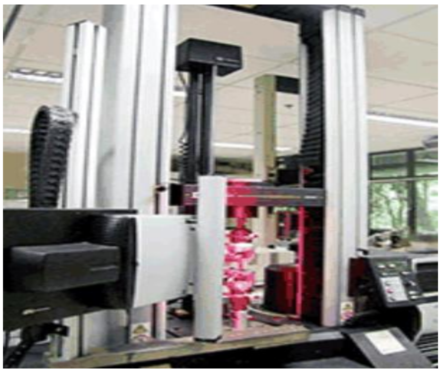

Fig. 2 Universal testing machine (5556, INSTRON)

4.1 Stiffness

The tire stiffness testing was conducted using the vertical stiffness tester, as illustrated in Figure 3. The pneumatic tire was affixed to the axle of the tester, and a flat surface ascended to compress the tire with the designated load. Three distinct vertical forces, namely 4,400 N, 4,600 N, and 4,900 N, derived from calculations based on vehicle weight and passengers, were applied for the testing. The inflation pressures were set at 220 kPa to examine the tire deformation behavior, a value recommended for this specific size of the pneumatic tire. This comprehensive testing approach allowed for a thorough analysis of the tire's stiffness characteristics under various loads and inflation pressures.

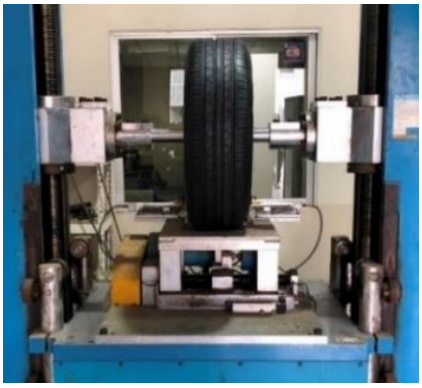

Fig. 3 Vertical stiffness testing of a 205/65 R15 pneumatic tire

4.2 Footprint

The investigation into the footprint of the 205/65

R15 tire under various loads involved conducting footprint tests under three different load conditions, all with the same inflation pressure. For this, a pressure measurement film (Prescale, Fuji) with a precision of ±10% was positioned on the moving surface of the vertical stiffness tester during the tire compression process. As a result, the film was pressed together with the tire, allowing for the visualization of the tire contact patch on the film, as depicted in Figure 4. The tire groove within this contact patch serves as a benchmark for the FEM, offering a reference point for further analysis and validation.

Fig. 4 Footprint of 205/65 R15 tire at an inflation pressure of 220 kPa and vertical force of 4,600 N

5. FINITE ELEMENT MODELING

The deformation of a pneumatic tire under an external load is dictated by specific equations that articulate the relationship between the applied load and resulting tire deflection. These equations serve as crucial tools in comprehending how a tire reacts to external forces as follows:

$$\frac{\partial \sigma_{ij}}{\partial x_i} + \gamma_i = 0, \quad (1)$$

$$\tau_i = \sigma_{ij} n_j, \quad (2)$$

where σ_{ij} denotes Cauchy stress, x_i denotes cartesian coordinate, γ_i denotes body force, and τ_i denotes the boundary traction component.

Equation (1) can be reformulated through the FEM as outlined in reference [11] by the following equations.

$$(\boldsymbol{K}_E + \boldsymbol{K}_G)\Delta v = \boldsymbol{f}_l + \boldsymbol{f}_{int}, \quad (3)$$

$$\boldsymbol{K}_E = \int \boldsymbol{B}^T C \boldsymbol{B} d\forall, \quad (4)$$

$$\boldsymbol{K}_G = \int \left(L_{jpk} \cdot \sigma_{ki}^0 \cdot L_{jqi} - 2B_{jpk} \cdot \sigma_{ki}^0 \cdot B_{jqi}\right) d\forall, \quad (5)$$

$$\boldsymbol{f}_l = \boldsymbol{f}_b + \boldsymbol{f}_{tract} = \int \boldsymbol{N}^T \gamma d\forall + \int \boldsymbol{N}^T \tau ds, \quad (6)$$

$$\boldsymbol{f}_{int} = \int \boldsymbol{B}^T \sigma d\forall, \quad (7)$$

where $\boldsymbol{K_E}$ denotes the elastic stiffness matrix, $\boldsymbol{K_G}$ denotes the geometry stiffness matrix, v denotes the nodal displacement, $\boldsymbol{f}_l$ denotes the external load vector, $\boldsymbol{f}_{int}$denotes the internal load vector, C denotes a constant over the element, $\boldsymbol{B}$ denotes the strain interpolation matrix, $\forall$ denotes the element volume, S denotes the element surface, L_{ipk} denotes the cartesian different operator, and $\boldsymbol{N}$ denotes the shape function matrix.

The constitutive model within FEA is encapsulated within the elastic stiffness matrix function. Given the nonlinear characteristics of tire materials, particularly the sidewall, a hyperelastic constitutive model was employed in the analysis. This model is elucidated through a strain energy function that correlates with the stress-strain characteristics of the material. In the current investigation, the Mooney-Rivlin hyperelastic constitutive model, as described in reference [13], was utilized to accurately represent the nonlinear response of tire deformation. The Mooney-Rivlin model is expressed as follows:

$$W = C_{10}(I_1 - 3) + C_{01}(I_2 - 3) \quad (8)$$

where $\boldsymbol{W}$ denotes strain energy function, C_{10} and C_{01} denote the material coefficient, and $\boldsymbol{I_1}$ and $\boldsymbol{I_2}$ denote invariant of the deviatoric strain.

The 205/65R15 tire was constructed by assembling various components, including the sidewall, bead wire, ply layers, and steel belts. The FE model of the tire was developed using a combination of 1D and 2D elements. Specifically, 2D quadratic axisymmetric elements were employed to model the side wall and bead wire, while 1D rebar elements were used to represent the ply layers and steel belts. These elements were meticulously arranged to replicate the tire section in accordance with the components of a 205/65R15 tire, as illustrated in Figure 5. The FE model of the 2D cross-section tire underwent rotation around an axis to generate the 3D FE model of the slick tire, as depicted in Figure 6(a). Subsequently, tire tread elements, constructed with tetrahedral elements, were assigned to make contact with the FE model of the slick tire using a glue contact type (Figure 6(b)). To simulate the stiffness test, a rigid surface was established and set to move upward, applying pressure to the FE model of the tire, as demonstrated in Figure 7.

The Mooney-Rivlin constitutive model was implemented to characterize the material behavior of the side wall and tread in the tire model, while the remaining components were defined using a linear isotropic material model. To ensure accuracy, the mesh quality was thoroughly verified, resulting in a total element counts of 290,769 for the FE model of the tire. The boundary conditions were set with pressure applied at the edge of elements and fixed

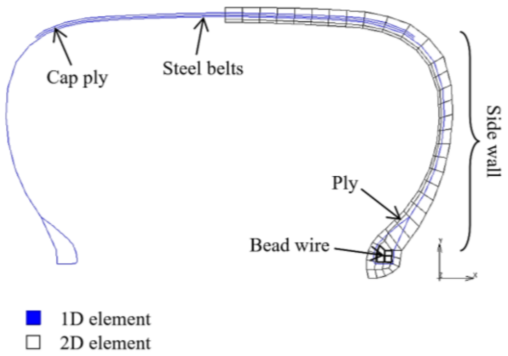

Fig. 5 The 2D cross-section of the tire

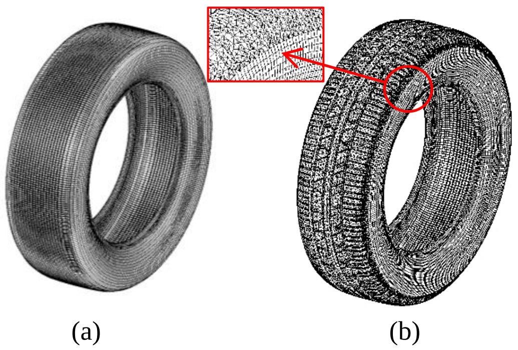

Fig. 6 (a) FE model of the slick tire and (b) FE model of the 205/65R15 tire

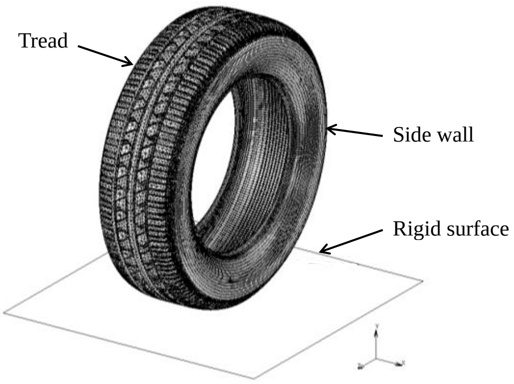

Fig. 7 FE model of tire stiffness testing

constraints at the rim location. Upon reaching the designated inflation pressure, a rigid surface was mobilized to move upward, applying the intended load to the FE model of the tire. The FEA results were then compared to experimental data, focusing on tire deformation and footprint. The FEA computations were executed on a personal computer equipped with a Core-i7 CPU and 8 GB of RAM.

6. RESULTS AND DISCUSSION

6.1 Tire Material Models

The Mooney-Rivlin model was employed to reconcile experimental data using the curve fitting method [14, 15], as depicted in Figure 8. This figure

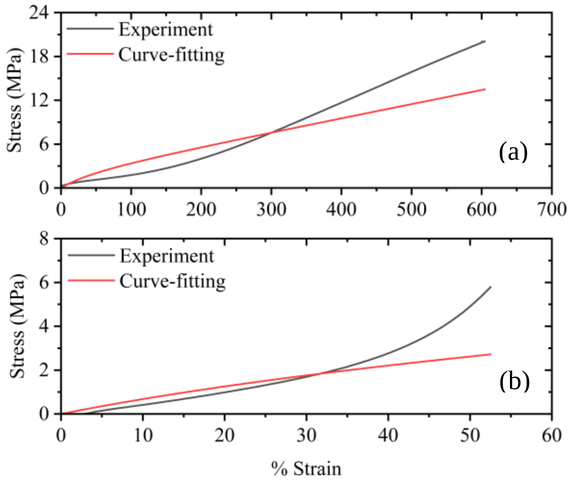

Fig. 8 Stress vs. % strain graphs of (a) tensile and (b) compression testing

Table 1 Mechanical properties of tire components

Tire component	Mechanical property (MPa)			
	C_{10}	C_{01}	E	ν
Sidewall (H)	1.246	2.9e-11	-	-
Tread (H)	0.136	0.661	-	-
Ply (L)	-	-	9,500	0.3
Cap ply (L)	-	-	3,000	0.3
Steel belts (L)	-	-	110,316	0.46
Bead wire (L)	-	-	200,000	0.3

Note: E denotes an elastic modulus, ν denotes a Poisson's ratio, C10 and C01 denote constant, H denotes the hypereslastic material, and L denotes the linear isotropic material.

juxtaposes the fitted curve with the actual experimental results, showcasing a high degree of agreement. The material properties of the tire in the FEA are detailed in Table 1, with R^2 values of 0.97 and 0.95 for the Mooney-Rivlin model applied to the sidewall and tread, respectively.

However, a noticeable deviation becomes evident at higher strain levels. It is crucial to emphasize that the primary deformation of the tire predominantly occurs at lower strain levels. Consequently, the analysis deliberately focused on this lower strain range for both the sidewall and tread components. By concentrating on the strain levels most relevant to typical operational conditions, the analysis seeks to provide a more accurate representation of the tire's behavior, even as it acknowledges and addresses discrepancies at higher strain levels.

Figures 9(a) and 9(b) depict strain values for a tire under maximum vertical load and inflation pressure, revealing sidewall strains below 100% and tread strains under 30%. The analysis deliberately focuses on the lower strain range to accurately capture the tire's behavior in realistic conditions. This emphasis recognizes that typical usage induces predominant deformation at lower strain levels. By staying within these bounds, the analysis aims to provide a precise understanding of the tire's response, ensuring relevance to practical operating scenarios and enhancing the overall utility of the findings.

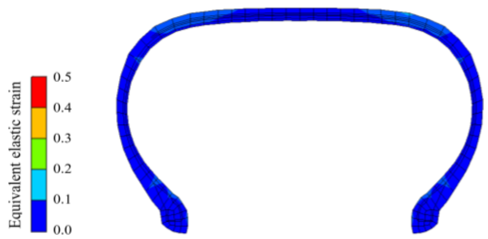

(a)

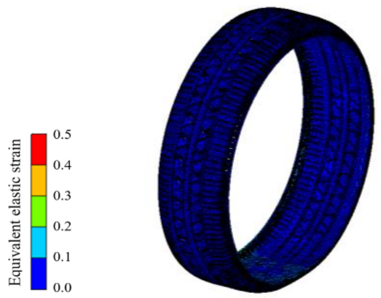

(b)

Fig. 9 Strain on (a) side wall and (b) tread

6.2 Validation of the Finite Element Model

Figure 10 displays the FEA results, showcasing a color contour that represents the tire displacement. The deformed tire's displacement is compared with experimental data under a consistent inflation pressure of 220 kPa and varying vertical loads. In Figure 11, the correlation between vertical load and displacement is presented. The FE model exhibits excellent agreement with the experimental results, with an average error of 6.47%. This suggests that the FEM reliably predicts tire displacement under different vertical loads, providing a solid representation of the tire's behavior in these conditions. The low average error percentage underscores the accuracy and dependability of the Finite Element Model in simulating tire deformation. Accurately determining the air volume within the contact area is crucial for gaining insights into tire

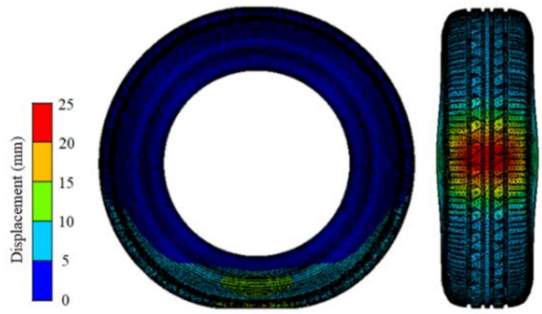

Fig. 10 Deformation of the tire at an inflation pressure of 190 kPa and a vertical force of 4400 N

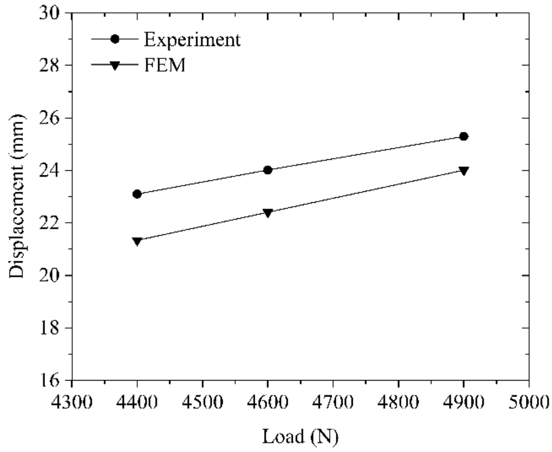

Fig. 11 Comparison of the vertical displacement results between the experiment and FEM

sound generation, especially concerning the air-borne mechanism associated with air pumping. The volume of air contained within this specific region plays a pivotal role in influencing the generation of sound.

To ensure a comprehensive characterization of the contact area, it is imperative to validate the FEA results through comparison with experimental data. The contact area delineates the region where the tire interacts with the rigid surface, as depicted in Figure12. Figures 13(a) to 13(c) showcase the enlargement of the contact area as the vertical load increases under an inflation pressure of 220 kPa. This evolution of the contact area is summarized in Figure 14. The comparison and synthesis of FEA and experimental data provide a robust foundation for understanding the variations in the contact area, contributing to a more accurate representation of the tire's interaction with the rigid surface.

In Figure 14, the relationship between the vertical load and the tire's footprint area is illustrated. Experimental measurements of the footprint area range from 94.64 mm² to 105.41 mm² under varying vertical load conditions. Notably, the maximum difference between the experimental measurements and the FEM predictions for the footprint area is

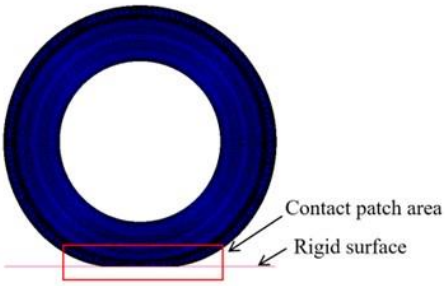

Fig. 12 Contact patch region between tire and rigid surface

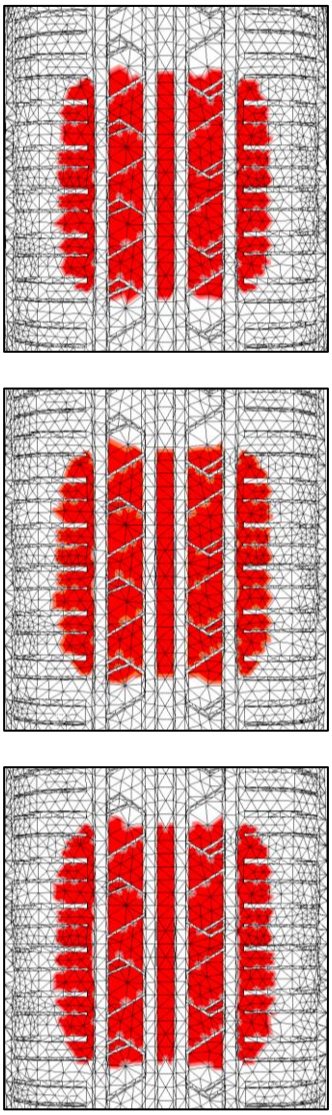

(a)

(b)

(c)

Fig. 13 Contact patch area by FEA at (a) 4400 N, (b) 4600 N, and (c) 4900 N

15.89%. This discrepancy provides valuable insights into the accuracy of the FEM in predicting changes in the footprint area as the vertical load varies, highlighting areas for potential refinement or further investigation in the model.

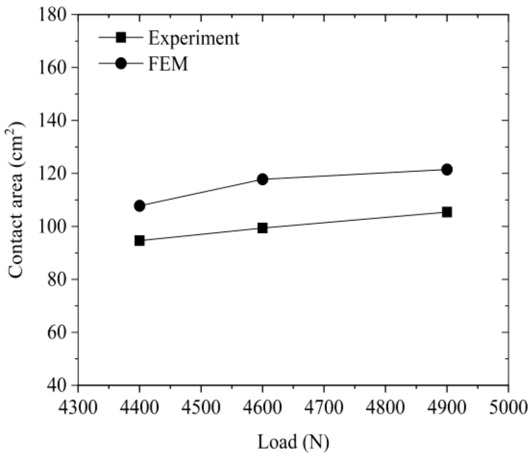

Fig. 14 Comparison of the contact area results between the experiment and FEM

While acknowledging some discrepancies between the experimental and FEA results, it's crucial to highlight the overall consistency in trends observed for both displacement and footprint area. Notably, as the load on the tire rises, both experimental and FEA findings consistently indicate an increase in tire displacement and footprint area. This suggests that, despite specific errors, the FEA model effectively captures the general behavior of the tire under varying load conditions. In the subsequent section, the FEA results will be employed to delineate the air volume within the contact patch area, contributing to a more comprehensive understanding of tire behavior.

6.3 Air volume analysis

The CAD software played a pivotal role in determining the air volume within the contact patch area. The tire contact area was enclosed by a rectangular prism with dimensions of 315×720×180 mm³ (width × length × height). Extracting the deformed tire from this prism, as illustrated in Figure 15, facilitated the calculation of the air volume at the contact patch area. Notably, this air volume exhibited a gradual increase with rising inflation pressure, while conversely decreasing with an increase in vertical load. The intricate relationship between tire pressure, vertical load, and air volume is illustrated in Figure 16.

To express this relationship, an air volume function is defined by Equation 9. This detailed analysis provides valuable insights into the dynamic interplay of inflation pressure, vertical load, and resulting air volume within the tire contact patch area.

$$V_a = -AP^2 + BP + C \tag{9}$$

where $\boldsymbol{V_a}$ denotes the air volume, $\boldsymbol{P}$ denotes the inflation pressure, and A, B, and C denote the model constants.

The trend of increasing air volume aligned with the rising inflation pressure, while the decrease in the

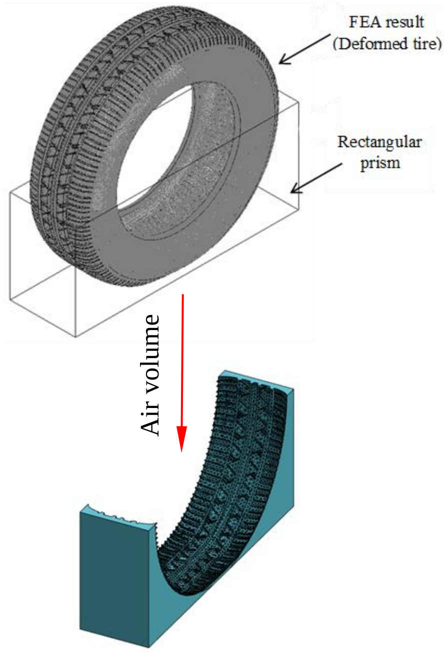

Fig. 15 The air volume extracted from the contact patch area

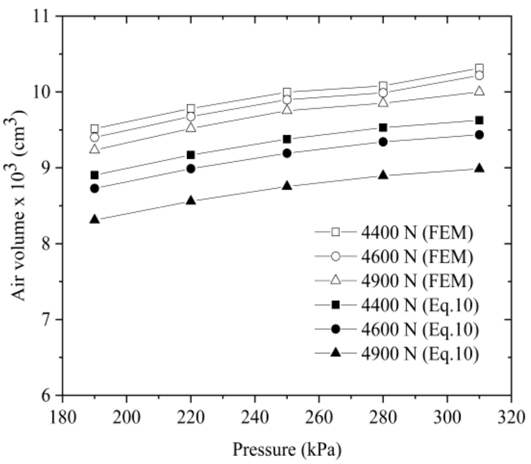

Fig. 16 The air volume at the contact patch area with different inflation pressure and vertical loads

air volume function correlated with the increasing vertical load. To model this relationship, the Cowper-Symonds model, as previously proposed in works [16-20], was employed. Consequently, the air volume function is formulated with two variables, namely inflation pressure and vertical load, represented by Eq. 10. This approach allows for a comprehensive representation of the intricate interdependence between inflation pressure, vertical load, and resulting air volume, enhancing the accuracy of the proposed model in describing the behavior of the tire under varying conditions.

$$\boldsymbol{V_a} = (-\boldsymbol{A}\boldsymbol{P}^2 + \boldsymbol{B}\boldsymbol{P} + \boldsymbol{C})\left(\mathbf{1} - \left(\frac{\boldsymbol{L}}{\boldsymbol{D}}\right)^{\frac{1}{\boldsymbol{P}}}\right) \qquad (\mathbf{10})$$

where $\boldsymbol{V_a}$ denotes the air volume, $\boldsymbol{P}$ denotes the inflation pressure, L denotes the vertical load, A, B, and C denote the model constants, and D and P denote the constant of Cowper-Symonds model.

In this study, the tire's inflation pressure underwent variations within the range of 190 kPa to 310 kPa, while the vertical load spanned from 4400 N to 4900 N. Table 2 provides the constants that define the proposed function. When comparing this function with Finite Element Analysis results, the average error was found to be less than 7.78%. This outcome underscores the efficacy of the proposed function in accurately approximating the intricate relationship between tire pressure and vertical load. The minimal average error further attests to the reliability of the model, validating its utility in capturing the dynamic behavior of the tire under diverse operating conditions.

Table 2 Constants of the proposed function

A	*B*	*C*	*D*	*P*
0.03	22.49	61.42	6,253.50	0.1062

7. CONCLUSION

This study aimed to explore the correlation between tire inflation pressure, vertical load, and air volume within the contact patch area of a deformed pneumatic tire interacting with the pavement, focusing on its relevance to airborne noise generation, specifically air pumping. Using the FEM, the accuracy of the FE model was assessed by comparing it to experimental data, revealing its reliable representation of tire behavior across diverse scenarios. Notably, the FE model demonstrated high accuracy, with an average error of 6.47% in vertical stiffness tests and 15.89% in footprint tests, confirming its dependability for understanding tire performance in various conditions. As tire load increased, both experimental and FEM predictions indicated noticeable rises in tire displacement and footprint area. The study also emphasized a significant relationship between tire pressure, vertical load, and air volume at the contact patch. Increasing tire pressure led to greater air volume due to inflation, while higher vertical load resulted in decreased air volume primarily due to tire deformation.

Based on these results, the study introduced an equation to assess air volume as a function of vertical load and inflation pressure, showing an average deviation of 7.78% when compared to FEA results. This underlines the equation's effectiveness in capturing the relationship between vertical load, inflation pressure, and air volume, serving as a reliable method for evaluating air volume changes in tires under diverse conditions. This equation's accuracy is validated by its close alignment with FEA results, emphasizing the significance of these parameters in influencing tire noise generation, particularly in the context of air-pumping noise.

In conclusion, this study makes a substantial contribution to the broader understanding of noise reduction techniques, providing a foundation for potential advancements and continued research. The insights gained offer valuable guidance for optimizing tire performance and developing effective noise reduction strategies in practical applications.

8. ACKNOWLEDGMENTS

This research was supported by funding from the National Research Council of Thailand (NRCT) and Siam Rubber Company Limited through the Research and Researchers for Industries (RRI) Master Scholarship, Grant No. N41A650167.

9. REFERENCES

[1] Nilsson N., On generating mechanisms for external tire noise. SAE Technical Paper, Vol. 112207630, 1976, pp.193-200.

[2] Li T., Burdisso R., Sandu C., Literature review of models on tire-pavement interaction noise. Journal of Sound and Vibration, Vol. 420, 2018, pp. 357-445.

[3] Keijiro I., and Ichiro Y., A study on the mechanism of tire/road noise. JSAE Review, Vol. 17, 1996, pp. 139-144.

[4] Sirin O., Ohiduzzaman M., and Kassem E., Influence of temperature on tire-pavement noise in hot climates: Qatar case. Case Studies in Construction Materials, Vol. 15, 2021, pp. 229-236.

[5] Prashanta G., Yousof A., and Abhilash J. C., An experimental and computational investigation of air-borne noise generation mechanisms in tires. Journal of Vibration and Control, Vol. 25, Issue 3, 2018, pp. 529-537

[6] Spies L., Li T., Burdisso R., Sandu C., An artificial neural network (ANN) approach to model Tire-Pavement interaction noise (TPIN) based on tire noise separation. Applied Acoustics, Vol. 206, 2023, pp. 109294.

[7] Marianne B. L. B., Julien C., and Philippe K., Tyre/road noise: A piston approach for CFD modeling of air volume variation in a cylindrical road cavity. Journal of Sound and Vibration, Vol. 469, 2020, pp. 115140.

[8] Zhou, H., Jiang, Z., Wang G., Qian H., and Qiao, L., The Analysis of a Sound-Generating Mechanism for Tire Pattern Groove Air Pumping by CFD. In: (SAE-China), S. (eds) Proceedings of the 19th Asia Pacific Automotive Engineering Conference & SAE-China Congress 2017: Selected Papers, Vol. 486, 2017, pp. 329-345.

[9] Liang C., Wang G., An D., and Ma Y., Tread Wear and Footprint Geometrical of Truck Bus Radial Tires. Chinese Journal of Mechanical Engineering, Vol. 26, Issue 3, 2013, pp. 506-511

[10] Zhou S, Chen L, Li Y, Sun P, Su G, Meng J., Study on the influence of different tire cord structures on tire grounding characteristics. Journal of Engineered Fibers and Fabrics, Vol. 17, 2022, pp. 1-11.

[11] Phromjan J, and Suvanjumrat C., Development of solid tire model for finite element analysis of compressive loading. Songklanakarin Journal of Science and Technology, Vol. 43, Issue 1, 2021, pp. 229-236.

[12] Phromjan J, and Suvanjumrat C., Vibration effect of two different tires on baggage towing tractors. Journal of Mechanical Science and Technology, Vol. 32, Issue 4, 2018, pp. 1539-1548.

[13] Bathe K. J., Finite element nonlinear analysis in solid and structural mechanics. Finite Element Procedures. Prentice Hall, 1996, pp. 485–641

[14] Phromjan J., and Suvanjumrat C., Material Characteristic for Capability Analysis of Solid Tire by Finite Element Method. Key Engineering Materials, Vol.777, 2018, pp. 416-420.

[15] Rugsaj R., and Suvanjumrat C., Finite Element Analysis of Hyperelastic Material Model for Non-Pneumatic Tire. Key Engineering Materials, Vol. 775, 2018, pp. 554–559.

[16] Phromjan J., and Suvanjumrat C., Non-pneumatic tire with curved isolated spokes for agricultural machinery in agricultural fields: Empirical and numerical study. Heliyon, Vol. 9, Issue 8, 2023, pp. e18984.

[17] Suvanjumrat C., and Puttapitukporn T., Determination of drop-impact resistance of plastic bottles using computer aided engineering. Kasetsart Journal (Natural Science), Vol. 45, Issue 5, 2011, pp. 932–942.

[18] Phromjan J., and Suvanjumrat C., Effects on spoke structure of non-pneumatic tires by finite element analysis. International Journal of Automotive Technology, Vol. 23, 2022, pp. 1437–1450.

[19] Loksupapaiboon K., and Suvanjumrat C., Forced convective heat transfer and fluid flow past a rotating hand-shaped former for improving rubber glove curing. Case Studies in Thermal Engineering, Vol. 47, 2023, pp. 103050.

[20] Chokngamvong S., and Suvanjumrat C., Study of drying kinetics and activation energy for drying a pineapple piece in the crossflow dehydrator. Case Studies in Thermal Engineering, Vol. 49, 2023, pp. 103351.